Reticulum II: Particle Dark Matter and Primordial Black Holes Limits

Thomas Siegert,[1]★ Celine Boehm,[2] Francesca Calore,[3] Roland Diehl,[4] Martin G. H. Krause,[5]
Pasquale D. Serpico,[3] and Aaron C. Vincent[6]

[1]*Institut für Theoretische Physik und Astrophysik, Universität Würzburg, Campus Hubland Nord, Emil-Fischer-Str. 31, 97074 Würzburg, Germany*
[2]*Sydney Consortium for Particle Physics and Cosmology, School of Physics, The University of Sydney, NSW 2006, Australia*
[3]*Univ. Grenoble Alpes, Univ. Savoie Mont Blanc, CNRS, LAPTh, F-74940 Annecy, France*
[4]*Max-Planck-Institut für extraterrestrische Physik, Gießenbachstraße, 85741 Garching b. München, Germany*
[5]*Centre for Astrophysics Research, Department of Physics, Astronomy and Mathematics, University of Hertfordshire, College Lane, Hatfield, Hertfordshire AL10 9AB, UK*
[6]*Department of Physics, Enigneering Physics and Astronomy, Queen's University, Kingston, ON, K7L 3N6, Canada*

ABSTRACT

Reticulum II (Ret II) is a satellite galaxy of the Milky Way and presents a prime target to investigate the nature of dark matter (DM) because of its high mass-to-light ratio. We evaluate a dedicated INTEGRAL observation campaign data set to obtain γ-ray fluxes from Ret II and compare those with expectations from DM. Ret II is not detected in the γ-ray band 25–8000 keV, and we derive a flux limit of $\lesssim 10^{-8}$ erg cm^{-2} s^{-1}. The previously reported 511 keV line is not seen, and we find a flux limit of $\lesssim 1.7 \times 10^{-4}$ ph cm^{-2} s^{-1}. We construct spectral models for primordial black hole (PBH) evaporation and annihilation/decay of particle DM, and subsequent annihilation of e^+s produced in these processes. We exclude that the totality of DM in Ret II is made of a monochromatic distribution of PBHs of masses $\lesssim 8 \times 10^{15}$ g. Our limits on the velocity-averaged DM annihilation cross section into e^+e^- are $\langle\sigma v\rangle \lesssim 5 \times 10^{-28} (m_{\rm DM}/{\rm MeV})^{2.5}$ cm^3 s^{-1}. We conclude that analysing isolated targets in the MeV γ-ray band can set strong bounds on DM properties without multi-year data sets of the entire Milky Way, and encourage follow-up observations of Ret II and other dwarf galaxies.

Key words: keyword1 – keyword2 – keyword3

1 INTRODUCTION

Siegert et al. (2016c) reported a 3.1σ signal of a 511 keV line from the direction of the dwarf galaxy Reticulum II (Ret II; distance $d = 30 \pm 2$ kpc; Koposov et al. 2015). The line flux from this previous work was extraordinarily high, $F_{511} = (1.7\pm0.5)\times10^{-3}$ ph cm^{-2} s^{-1}, which would make Ret II the most luminous 511 keV source in the sky. The signal has been interpreted in terms of a recent binary neutron star (NS) merger (Fuller et al. 2018), possibly outshining the entire galaxy. Ret II has also been reported to show an excess at GeV energies (Geringer-Sameth et al. 2015) which might point to a dark matter (DM) origin of the signal. Follow-up analyses found no flux enhancement above the diffuse GeV emission (Albert et al. 2017). Intrigued by these finding, the INTEGRAL (Winkler et al. 2003) satellite performed a dedicated observation campaign to follow up the signal. In this work, we analyse the new 1 Ms data together with archival data from the coded-mask γ-ray spectrometer onboard INTEGRAL, SPI (Vedrenne et al. 2003). We use our findings to set limits on possible DM models, including primordial black holes (PBHs) and annihilation or decay of (light) DM particles.

This paper is structured as follows: In Sec. 2, we describe the new observations, and how SPI data are analysed in general. We build photon-emission models expected from the evaporation of PBHs and annihilating/decaying particle DM in Sec. 3. Here, we also include the possible annihilation of positrons (e^+s) as a DM product into the galaxy emission spectra. Our results are presented in Sec. 4. We conclude in Sec. 5.

2 NEW OBSERVATION CAMPAIGN

The previous analysis by Siegert et al. (2016c) focussed on the search of 511 keV signals from the 39 satellite galaxies of the Milky Way (MW) known at the time. In their data set, the entire sky was modelled and the diffuse 511 keV emission from the MW itself was included. Before the new observation campaign, Ret II had never been targeted for observations by SPI because 1) the galaxy was only discovered in 2015 (Koposov et al. 2015), and 2) other known X- or γ-ray sources are separated from Ret II by at least 18°. However, thanks to SPI's wide fully-coded field of view (FCFOV) of 16° × 16° (30° × 30° partially coded), Ret II data were collected also before its discovery. Outside the full coding region, the effective area of the instrument sharply drops which placed previous Ret II observations right onto exposure edges with a cumulative on-target observation time of 550 ks, split over ten years. While these effect were taken into account in the analysis, dedicated observations, pointed directly to Ret II, would be suitable to validate earlier findings.

★ E-mail: tho.siegert@gmail.com

2.1 Data Set

Our new data set includes previous observations between 2003 and 2013 and adds ∼ 1 Ms during the Ret II campaign in 2018. We selected all pointed observations (pointings) whose distance to Ret II is less than 16° so that our target is always in the FCFOV. This amounts to 603 pointings with an average observation time of 3300 s each. The mean dead time of a working detector is about 18.2 %. Since the launch of the INTEGRAL mission in October 2002, four of the 19 SPI detectors have failed, reducing the effective area by ≈ 20 %. The total dead-time- and efficiency-corrected exposure time then amounts to 1.38 Ms. We use SPI's bandpass between 25 and 8000 keV, and perform our analysis in 29 logarithmic energy bins, plus a single narrow bin for the 511 keV line from 508 to 514 keV.

2.2 General Analysis Method

SPI data analysis relies on the comparison of expected detector illuminations, that is, patterns in the 19-detector data space, with the measured count rate per pointing and energy. Fluxes are estimated by maximising the Poisson likelihood,

$$\mathcal{L}(D|M) = \prod_p \frac{m_p^{d_p} \exp(-m_p)}{d_p!}, \tag{1}$$

where d_p are the measured counts in pointing p, and m_p is the model expectation. MeV γ-ray measurements are described by a two component model, one representing the instrumental background m^{BG}, and one representing the celestial emission m^{SKY}. Instrumental background originates from cosmic-ray interactions with the satellite material and leads to continuum (C) and line (L) backgrounds (Diehl et al. 2018). Spatial emission models are convolved with the imaging response function of SPI, that is, the mask coding, leading to a 19-element vector of expected source counts for each pointing. The total model reads

$$\begin{aligned} m_p &= m_p^{\mathrm{BG}} + m_p^{\mathrm{SKY}} = \\ &= \sum_{t,t'} \left[\sum_{i \in \{C,L\}} \beta_{i,t} R_{p,i}^{\mathrm{BG}} + \sum_{j=1}^{N_S} \alpha_{j,t'} R_{p;lb}^{\mathrm{SKY}} M_j^{lb}(\boldsymbol{\phi_j}) \right], \tag{2} \end{aligned}$$

where $R_{p,i}^{\mathrm{BG}}$ is the background model (response) appropriate for pointing p, scaled by the amplitudes $\beta_{i,t}$ for background components $i \in \{C, L\}$ varying on timescales t, $R_{p;lb}^{\mathrm{SKY}}$ is the coded-mask response in pointing p, converting the $j = 1 \dots N_S$ sky models $M_j^{lb}(\boldsymbol{\phi})$ from image space lb to the data space.

The source models may have additional parameters $\boldsymbol{\phi_j}$, for example defining the position of point sources, and are scaled by the amplitudes $\alpha_{j,t'}$, possibly varying on another time scale t'. Given SPI's angular resolution of 2.7°, and the expected maximum extent of Ret II's DM halo of 1°, we model the galaxy as point source,

$$M_{\mathrm{Ret\,II}}(l, b) = \delta(l - l_0)\delta(b - b_0), \tag{3}$$

with the Galactic coordinates of Ret II $(l_0, b_0) = (266.30, -49.74)$. All other sources that can be expected in our data set, EXO 0748-676, ESO 33-2, SMC X-1, and LMC X-4 are modelled as point sources as well. The fitted parameters in Eq. (2) are $\beta_{i,t}$ and $\alpha_{j,t'}$. The fit is performed with `spimodfit` (Halloin 2009), which creates a spectrum by looping over the energy bins defined in our data set. Details about the procedure are found in Siegert et al. (2019).

2.3 Spectral Fitting

The spectrum created in this way is subject to the instrument dispersion, that is, the probability that a photon with initial energy E_i is measured at a final energy E_f owing to scattering in the instrument. In order to correct for the intrinsic dispersion, expected spectral models $\frac{dF}{dE}$ are convolved with the energy-redistribution matrix $H(E_i, E_f)$ that forward-folds the models into the appropriate data space. Thus, the spectral models read

$$\frac{dF(E_f; \boldsymbol{\psi})}{dE_f} = \int dE_i H(E_i, E_f) \frac{dF(E_i; \boldsymbol{\psi})}{dE_i}, \tag{4}$$

with $\frac{dF}{dE_f}$ being the folded model which is compared to the extracted flux values from Sec. 2.2, and $\frac{dF}{dE_i}$ is the intrinsic source model that depends on a set of spectral parameters $\boldsymbol{\psi}$. We use the Multi-Mission-Maximum-Likelihood (3ML, Vianello et al. 2015) framework to perform spectral fits. Details about the choices of prior probabilities and parameter ranges are given in Appendix A.

We note that, ideally, the steps explained in Secs. 2.2 and 2.3 should be performed in one single step to enhance the sensitivity of the parameter estimation, which is, however, not yet implemented in the current software release.

3 EXPECTATIONS IN THE MEV BAND

No MeV emission has ever been detected from a (dwarve) satellite galaxy. Therefore, the expected signals have a large variety, ranging from γ-ray line emission due to radioactive decays and (subsequent) e^+ emission. Population synthesis models estimate a 1.8 MeV γ-ray line flux from the decay of ^{26}Al of the order of 10^{-6} ph cm^{-2} s^{-1} from the Large Magellanic Cloud (LMC), about one order of magnitude below SPI's sensitivity Diehl et al. (2018). Because the expected line flux is related to the star formation and supernova rate, any other satellite galaxy, and in particular Ret II, can be expected to show no significant excess at 1.8 MeV. Cordier et al. (2004) performed a search for a 511 keV line owing to dark matter annihilation/decay from the Sgr dwarve galaxy, but found no excess. Siegert et al. (2016c) extended this search to all satellite galaxies of the MW, which resulted in one 3σ signal from the direction of Ret II out of 39 tested galaxies. Where this signal, if true, comes from is unknown, and might point to different origins in terms of NS mergers (Fuller et al. 2018), accreting X-ray binaries (Siegert et al. 2016a), or DM (Boehm et al. 2004). All these scenarios would show additional emission features in the MeV band besides a sole 511 keV line. In particular additional broad γ-ray lines from other nucleosynthesis products in NS mergers, continuum emission from a population of X-ray binaries, or radiative corrections in the final products from DM decay/annihilation or PBH decay. Therefore, we extract the spectrum of Ret II and nearby sources using the logarithmic energy binning defined in Sec. 2.1, plus a single bin for the 511 keV line. In this way, we can assess the previously found signal from Ret II in a model-independent fashion, and determine model dependent parameters using the additionally-expected components in Sec. 3.1.

3.1 Modelling the MeV Band in Ret II

We focus on the γ-ray spectra expected from the evaporation of PBHs in the mass range 10^{14}–10^{18} g and annihilating/decaying particle DM in the mass range 0.05–300 MeV. Other signals, for example the γ-ray emission from old NS mergers remnants, are not part of our predictions because the expected emission of one 10 kyr old remnant

Model	κ	M	n	ψ
PBH	f_{PBH}	M_{BH}	$1 \rightarrow D$	$\{f_{\mathrm{Ps}}, E_{\mathrm{kin}}^{\mathrm{max}}\}$
DM Annihilation	$\langle \sigma v \rangle$	$2m_{\mathrm{DM}}$	$2 \rightarrow J$	$\{f_{\mathrm{Ps}}, E_{\mathrm{kin}}^{\mathrm{max}}\}$
DM Decay	$1/\tau$	m_{DM}	$1 \rightarrow D$	$\{f_{\mathrm{Ps}}, E_{\mathrm{kin}}^{\mathrm{max}}\}$

Table 1. Parameters for considered DM models in Eq. (5).

in Ret II is about one million times lower (Korobkin et al. 2020) than the instrument sensitivity. While emission from GeV DM would also imprint in the MeV band, SPI is most sensitive to annihilation/decay to e^+e^- and subsequent emission processes considering the final state radiation (FSR) of the pairs as well as the annihilation of e^+s during propagation and after thermalisation. Therefore, we restrict our models to the two channels e^+e^- and $\gamma\gamma$, and present one $\mu^+\mu^-$ example for comparison. We follow the formalism of Fortin et al. (2009) throughout the paper.

The emission from DM haloes is described by a 'particle physics' and an 'astrophysics' component as

$$\frac{dF_\gamma (E_\gamma; \kappa, M, \psi, n)}{dE_\gamma} = \underbrace{\frac{\kappa}{4\pi M} \frac{dN_\gamma (E_\gamma; \psi)}{dE_\gamma}}_{\text{particle physics: PBH or DM}} \underbrace{\int_{\mathrm{los}} dr d\Omega \rho_{\mathrm{halo}}^n (r, \Omega)}_{\text{astrophysics: D or J}},$$

(5)

where κ, M, and ψ describe the parameters of interest for the specific cases of PBH evaporation, self-conjugated DM annihilation or decay (see Tab. 1), and the last term is the D- ($n = 1$) or J-factor ($n = 2$) of the galaxy. They describe the extent of the emission, calculated by an integration of the galaxy's halo profile $\rho_{\mathrm{halo}}(r, \Omega)$ over the line of sight (los). The photon spectrum $\frac{dN_\gamma(E_\gamma; \psi)}{dE_\gamma}$ is related to the photon density of states as $\frac{1}{N_\gamma}\frac{dN_\gamma}{dE_\gamma} = \frac{1}{\kappa}\frac{d\kappa}{dE_\gamma}$ so that the number of emitted photons per process is $N_\gamma = \int dE_\gamma \frac{dN_\gamma}{dE_\gamma}$. N_γ is thus normalising the source spectrum, Eq. (5), in terms of the totally-emitted photons.

We use the range of D- and J-factors of Ret II from the literature (Bonnivard et al. 2015; Evans et al. 2016; Albert et al. 2017), in particular $D \approx (1-4) \times 10^{18}$ GeV cm^{-2}, and $J \approx (0.2-3.7) \times 10^{19}$ GeV^2 cm^{-5}. The conversion of the D- and J-factor into other often-used units are $D = (0.9-3.5) \times 10^{-2}$ M$_\odot$ pc^{-2} = $(1.9-7.3) \times 10^{-6}$ g cm^{-2}, and $J = (0.6-8.4) \times 10^{-3}$ M$_\odot^2$ pc^{-5} = $(0.8-11.8) \times 10^{-29}$ g^2 cm^{-5}. We use these ranges as uniform priors in our spectral fits to include uncertainties in the DM halo as well as the distance to Ret II. Depending on the DM model, the parameters of interest change and are listed in Tab. 1. Here, f_{PBH} is the fraction of DM made of PBHs (unitless), $\langle \sigma v \rangle$ is the velocity-averaged DM annihilation cross section in units of cm^3 s^{-1}, $\tau = \Gamma^{-1}$ is the decay time of a DM particle in units of s, M_{BH} is the mass of PBHs in units of g, and m_{DM} is the DM particle mass in units of keV. The additional spectral model parameters $\psi = \{f_{\mathrm{Ps}}, E_{\mathrm{kin}}^{\mathrm{max}}\}$ appear when e^+ annihilation is included (see below).

3.1.1 Primordial Black Hole Evaporation

The spectrum of an evaporating black hole (BH) of mass M_{BH} due to Hawking radiation (Hawking 1975; Page & Hawking 1976) is

$$\left(\frac{dN_i}{dE_i}\right)_{\mathrm{BH}} = \frac{1}{2\pi} \frac{\Gamma_i (E_i, M_{\mathrm{BH}})}{\exp\left(\frac{E_i}{T_{\mathrm{BH}}}\right) - (-1)^{2s_i}}.$$

(6)
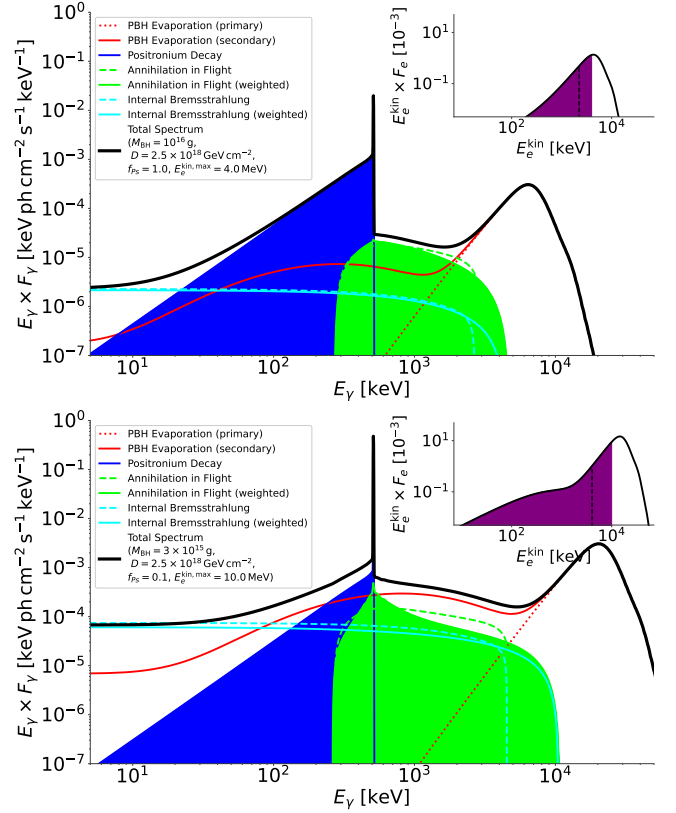
Figure 1. Expected γ-ray spectra from PBH evaporation and subsequent annihilation of positron-electron pairs, plus internal bremsstrahlung of emitted pairs. The two panels show different model parameters (see legends) for a D-factor of 2.5×10^{18} GeV cm^{-2}, consistent with Reticulum II. The small insets show the distribution of electrons and positrons from evaporation, together with the maximum kinetic energy $E_{\mathrm{kin}}^{\mathrm{max}}$ considered by the shaded area, and the mean kinetic energy of the electron/positron population (dashed line). The shaded area of the electron/positron distribution corresponds to the shaded areas in the γ-ray spectra.

In Eq. (6), E_i is the energy of particle i and s_i its spin. $\Gamma_i (E_i, M_{\mathrm{BH}})$ is the 'greybody' factor that alters the expected blackbody distribution of possible emitted particles, given the BH temperature

$$T_{\mathrm{BH}} = \frac{\hbar c^3}{8\pi G k_B M_{\mathrm{BH}}} = 6 \times 10^{-8} \left(\frac{M_\odot}{M_{\mathrm{BH}}}\right) \mathrm{K} = 1.06 \left(\frac{10^{16} \mathrm{g}}{M_{\mathrm{BH}}}\right) \mathrm{MeV},$$

(7)

where $\hbar$ is reduced Planck's constant, G is the gravitational constant, c is the speed of light, and k_B is Boltzmann's constant.

We use BlackHawk (Arbey & Auffinger 2019) to calculate the spectra of all relevant particles in the energy range between 1 keV and 1 GeV. BlackHawk allows to include secondary particle production due to hadronization, fragmentation, decay, and other processes as a result of BH evaporation, which we add to our spectra.

The production of e^+s from BH evaporation has no kinematic threshold based on the mass of the BG. However, the number of e^+s produced that may annihilate subsequently can lead to a 20–8000 keV flux stronger than the evaporation signal itself which is given by a BH mass of $\lesssim 1.1 \times 10^{17}$ g. Given the particle spectrum of e^+s from BlackHawk, the differential e^+ flux in a galaxy with D-factor D is given by

$$\frac{dF_e}{dE_e} = \frac{1}{4\pi M_{\mathrm{BH}}} \frac{dN_e}{dE_e} D,$$

(8)

so that the total possible e^+e^--annihilation flux F_{Ann} in that galaxy is

$$F_{\mathrm{Ann}} = \int_0^{E_{\mathrm{kin}}^{\max}} dE_{\mathrm{kin}} \frac{dF_e}{dE_{e,\mathrm{kin}}} \,. \tag{9}$$

Here, $E_{\mathrm{kin}}^{\max}$ is the maximum kinetic energy of a e^+ that annihilates within the galaxy and does not escape into the intergalactic medium. For the MW, $E_{\mathrm{kin}}^{\max}$ has been estimated to be around 3–7 MeV (Beacom & Yüksel 2006; Sizun et al. 2006). We caution, however, that these estimates may be inaccurate because the statistical methods to compare the expected spectrum with the measurements of two different instruments are not rigorously correct. Therefore, we leave $E_{\mathrm{kin}}^{\max}$ as a free parameter in our spectral fits. Because the transport and environmental conditions in Ret II are largely unknown, this procedure effectively takes into account these uncertainties. For reference, we discuss the two extreme cases of no and maximal e^+ annihilation in our results, Sec. 4, together with the intermediate solution of marginalising over $E_{\mathrm{kin}}^{\max}$.

The total annihilation flux is composed of three components,

$$F_{\mathrm{Ann}} = F_{511} + F_{\mathrm{oPs}} + F_{\mathrm{IA}}, \tag{10}$$

where F_{511} is the flux in the 511 keV line due to direct annihilation with e^-s and intermediate formation of Positronium (Ps), F_{oPs} is the three-photon decay flux of ortho-Ps, and F_{IA} is the total flux of e^+s annihilating in flight (IA) before stopping/thermalising.

The ortho-Ps and the line flux are related by quantum statistics as

$$F_{\mathrm{oPs}} = \frac{9 f_{\mathrm{Ps}}}{8 - 6 f_{\mathrm{Ps}}} F_{511} =: r_{32} F_{511}, \tag{11}$$

with f_{Ps} being the Ps fraction, that is, the number of e^+s forming Ps before annihilating (Leventhal et al. 1978). The scaling factor r_{32} ranges between 0 ($f_{\mathrm{Ps}} = 0$) and 4.5 ($f_{\mathrm{Ps}} = 1$). In general f_{Ps} depends on the annihilation conditions, for example the gas in which e^+s annihilate, which is a function of the temperature, density, and ionisation fraction, among others (e.g., Jean et al. 2006; Churazov et al. 2005, 2011; Siegert et al. 2016b). Since the true conditions in Ret II are unknown, we leave f_{Ps} as free parameters in our spectral fits. The ortho-Ps spectrum $\left(\frac{dN_\gamma}{dE_\gamma}\right)_{\mathrm{oPs}}$ has been calculated by Ore & Powell (1949), and we model the 511 keV line, $\left(\frac{dN_\gamma}{dE_\gamma}\right)_{511}$ as a Gaussian at 511 keV with a width according to SPI's energy resolution (Diehl et al. 2018; Attié et al. 2003).

Beacom & Yüksel (2006) derived a relation between F_{IA} and the 511 keV line flux,

$$F_{\mathrm{IA}} = \frac{1}{1 - \frac{3}{4} f_{\mathrm{Ps}}} \frac{1 - P}{P} F_{511} =: r_{\mathrm{IA}} F_{511}, \tag{12}$$

where $P = P(E_{\mathrm{kin}}, m_e)$ is the probability of a e^+ with initial kinetic energy E_{kin} to annihilate before stopping/thermalising. Therefore, the total annihilation flux can be expressed as

$$F_{\mathrm{Ann}} = (1 + r_{32} + r_{\mathrm{IA}}) F_{511}. \tag{13}$$

The survival probability in Eq. (12) is given in general by

$$P(E_{\mathrm{kin}}, m_e) = \exp\left(-n_X \int_{m_e}^{E_{\mathrm{kin}}} dE \frac{\sigma(E)}{\left|\frac{dE(E, n_X)}{dx}\right|}\right), \tag{14}$$

where $\sigma(E)$ is the total annihilation cross section, and $\left|\frac{dE(E, n_X)}{dx}\right|$ is the stopping power (energy loss rate, cooling function) of a e^+ propagating in a medium with density n_X. For simplicity, we only consider Coulomb losses which are expected to dominate up to 100 MeV for

MW-like conditions, $\left|\frac{dE(E, n_X)}{dx}\right|_{\mathrm{Coulomb}} \propto n_X$, so that n_X cancels. The total IA spectrum for mono-energetic injection of e^+s thus reads

$$\left(\frac{dF_\gamma}{dE_\gamma}\right)_{\mathrm{IA}}^{\mathrm{mono}} = F_{511} \frac{1}{1 - \frac{3}{4} f_{\mathrm{Ps}}} \frac{1}{P} \left(\frac{dN_\gamma}{dE_\gamma}\right)_{\mathrm{IA}}, \tag{15}$$

with

$$\left(\frac{dN_\gamma}{dE_\gamma}\right)_{\mathrm{IA}}^{\mathrm{mono}} = \frac{n_X}{2 m_e} \int_{E_1}^{E_{\mathrm{kin}}} dE \frac{P(E_{\mathrm{kin}}, E) \frac{d\sigma(E, E_\gamma)}{dE}}{\left|\frac{dE(E, n_X)}{dx}\right|}. \tag{16}$$

where the integration limit $E_1 = \max\left(\frac{(E_\gamma - m_e)^2 + E_\gamma^2}{(E_\gamma - m_e) + E_\gamma} m_e, E_\gamma\right)$ is bound to obey energy conservation (Svensson 1982; Beacom & Yüksel 2006). We note that $\int dE_\gamma \left(\frac{dN_\gamma}{dE_\gamma}\right)_{\mathrm{IA}} = 1 - P$. Since in the case of PBHs, the injection energy is not mono-energetic, we calculate a weighted photon spectrum given the distribution of kinetic energies from `BlackHawk` as

$$\left(\frac{dN_\gamma}{dE_\gamma}\right)_{\mathrm{IA}} = \frac{\int_0^{E_{\mathrm{kin}}^{\max}} dE_{\mathrm{kin}} \frac{dN_e}{dE_e} \left(\frac{dN_\gamma(E_{\mathrm{kin}})}{dE_\gamma}\right)_{\mathrm{IA}}^{\mathrm{mono}}}{\int_0^{E_{\mathrm{kin}}^{\max}} dE_{\mathrm{kin}} \frac{dN_e}{dE_e}}. \tag{17}$$

Radiative corrections in the production of e^+e^--pairs can be described as internal bremsstrahlung (IB) which can be calculated without detailed knowledge of the previous process. This final state radiation (FSR) arises as a result of the production itself and is independent of the astrophysical environment. The photon source spectrum of IB per 511 keV line photon is given by Beacom et al. (2005),

$$\left(\frac{dF_\gamma}{dE_\gamma}\right)_{\mathrm{IB}}^{\mathrm{mono}} = \frac{1}{2} \frac{1}{1 - \frac{3}{4} f_{\mathrm{Ps}}} \left(\frac{dN_\gamma}{dE_\gamma}\right)_{\mathrm{IB}}^{\mathrm{mono}}, \tag{18}$$

with

$$\left(\frac{dN_\gamma}{dE_\gamma}\right)_{\mathrm{IB}}^{\mathrm{mono}} = \frac{\alpha}{2\pi} \left[\frac{M^2 + (M - 2E_\gamma)^2}{M^2 E_\gamma} \ln\left(\frac{M(M - 2E_\gamma)}{m_e^2}\right)\right], \tag{19}$$

where here, $M = E_{\mathrm{kin}} + m_e$ is the particles' injection energy from PBH evaporation. Because the e^+-injection spectrum is again not mono-energetic, we weight over expected energy distribution such that

$$\left(\frac{dN_\gamma}{dE_\gamma}\right)_{\mathrm{IB}} = \frac{\int_0^{E_{\mathrm{kin}}^{\max}} dE_{\mathrm{kin}} \frac{dN_e}{dE_e} \left(\frac{dN_\gamma(E_{\mathrm{kin}})}{dE_\gamma}\right)_{\mathrm{IB}}^{\mathrm{mono}}}{\int_0^{E_{\mathrm{kin}}^{\max}} dE_{\mathrm{kin}} \frac{dN_e}{dE_e}}. \tag{20}$$

Finally, the total photon source spectrum of PBH evaporation including subsequent e^+-annihilation and IB in a galaxy is the sum the components:

$$\left(\frac{dF_\gamma}{dE_\gamma}\right)_{\mathrm{PBH}}^{\mathrm{tot}} = \left(\frac{dF_\gamma}{dE_\gamma}\right)_{\mathrm{PBH}} + \left(\frac{dF_\gamma}{dE_\gamma}\right)_{\mathrm{IB}} + \left(\frac{dF_\gamma}{dE_\gamma}\right)_{\mathrm{Ann}} =$$
$$= \left(\frac{dF_\gamma}{dE_\gamma}\right)_{\mathrm{PBH}} + \left(\frac{dF_\gamma}{dE_\gamma}\right)_{\mathrm{IB}} + \sum_{i \in \mathscr{A}} \left(\frac{dF_\gamma}{dE_\gamma}\right)_i, \tag{21}$$

with $\mathscr{A} = \{511, \mathrm{oPs}, \mathrm{IA}\}$. $\left(\frac{dF_\gamma}{dE_\gamma}\right)_{\mathrm{PBH}}$ is a function of M_{BH}, D and f_{PBH}, and $\left(\frac{dF_\gamma}{dE_\gamma}\right)_{\mathrm{Ann}}$ is a function of f_{Ps} and $E_{\mathrm{kin}}^{\max}$. We show two examples of the total emission spectrum from PBH evaporation in Ret II in Fig. 1.

3.1.2 Particle Dark Matter Annihilation and Decay

We consider light ($m_{\mathrm{DM}} \lesssim 300\,\mathrm{MeV}$) DM particles that either annihilate or decay directly into standard model particles, leading to an expected photon emission spectrum. Therefore we evaluate the cases
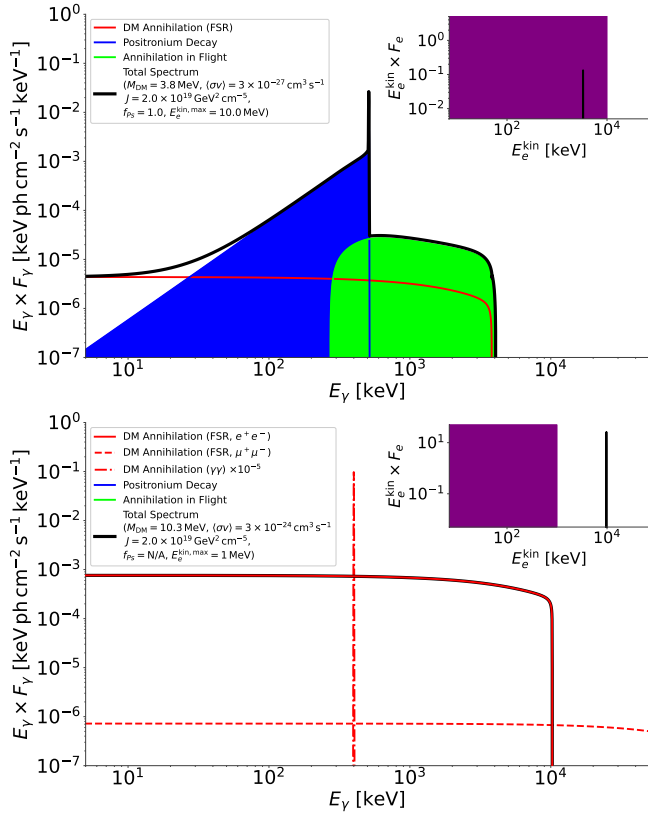
Figure 2. Expected γ-ray spectra from light dark matter annihilation and subsequent annihilation of positron-electron pairs, similar to Fig. 1. The two panels show different model parameters (see legends) for a J-factor of $2 \times 10^{19}\,\text{GeV}^2\,\text{cm}^{-5}$. The lower panel also shows model expectations from final state radiation of the $\mu^+\mu^-$-channel and direct decay into two photons.

(i) $\text{DM} + \text{DM} \rightarrow e^+ + e^- + (\gamma)_{\text{FSR}}$,
(ii) $\text{DM} + \text{DM} \rightarrow \gamma + \gamma$,
(iii) $\text{DM} \rightarrow e^+ + e^- + (\gamma)_{\text{FSR}}$,
(iv)   (a) $\text{DM} \rightarrow \gamma + \gamma$, and
    (b) $\text{DM} \rightarrow Y + \gamma$,

where Y is any relativistic particle, for example a sterile neutrino that decays into $\gamma + \nu$. The photon spectra of the FSR in cases 1. and 3. are identical to the IB spectrum,

$$\left(\frac{dN_\gamma}{dE_\gamma}\right)_{\text{FSR}} \equiv \left(\frac{dN_\gamma}{dE_\gamma}\right)_{\text{IB}}, \tag{22}$$

however now, $M = 2m_{\text{DM}}$ for annihilation and $M = 1m_{\text{DM}}$ for decay. Another factor of $\frac{1}{2}$ is required in Eq. (19) for Dirac DM annihilation/decay to account for distinct particle-antiparticle DM with equal densities. The expected photon spectrum of direct annihilation/decay into two photons (cases 2. and 4.) is a delta-function,

$$\left(\frac{dN_\gamma}{dE_\gamma}\right)_{\gamma\gamma} = 2\delta\left(E_\gamma - \frac{M}{2}\right). \tag{23}$$

Case 4. (b) differs from case 4. (a) only by an additional factor of 2. We model Eq. (23) as Gaussians with the energy resolution of SPI.

Similar to the PBH case, the emitted e^+s from DM particles in a galaxy's halo might annihilate during (IA) and after (Ps) propagation in the galaxy, or escape into the intergalactic medium if their injection energy is larger than a threshold $E_{\text{kin}}^{\text{max}}$. The only difference is now that the energy distribution of produced pairs is mono-energetic, so that either all or none of the pairs lead to additional e^+-annihilation

related spectra. Given the equivalence in Eq. (22), one can estimate the total 511 keV line flux from DM particle annihilation as

$$F_{511}^{\text{Ann}} = \left(1 - \frac{3}{4}f_{\text{Ps}}\right)\frac{J\langle\sigma v\rangle}{2\pi m_{\text{DM}}^2}, \tag{24}$$

and from DM particle decay as

$$F_{511}^{\text{Dec}} = \left(1 - \frac{3}{4}f_{\text{Ps}}\right)\frac{D}{2\pi m_{\text{DM}}\tau}. \tag{25}$$

The remaining spectral components from ortho-Ps and annihilation in flight are the same as in Sec. 3.1.1, except that now the mono-energetic cases are considered. The total source photon spectrum is again the sum of the components, here FSR, 511 keV line, ortho-Ps, and in-flight annihilation. We show examples of the expected DM annihilation spectra in Fig. 2.

4 RESULTS

We examine our model fits to measured data through a careful analysis of the residuals in different data space dimensions. Herein, it proves valuable to apply a back-projection onto the sky of the count residuals. For cases of background model imperfections, we would discover irregular or large-scale patterns on the sky, whereas for imperfections of the sky model (e.g., missing a point source) would show up as a single peak at the source's location. In Fig. 3, we show the residual count map of an instrumental-background-only fit in three example energy bands. Only the high-mass X-ray binary LMC X-4 is detected with a significance of 21σ up to an energy of $\sim 200\,\text{keV}$. The other sources, and in particular Ret II, are not seen in any energy band. The count residuals show no strong patterns as expected from an otherwise empty field. In the 511 keV band, the residuals appear more structured, which is a result of the reduced count rate compared to other bands. For reference, the particularly bright spot between ESO 33-2 and LMC X-4 at $(l, b) = (-78°, -37°)$ has a significance of $\sim 2.5\sigma$, and is thus considered a background fluctuation. Details about the 511 keV line from Ret II are given in Sec. 4.2.

4.1 Total Spectrum

We show the spectrum measured by SPI from the direction of Ret II, spatially modelled as a point source, Eq. (3), in Fig. 4. Because the source is not detected in any of the energy bins, we plot 2σ upper limits. For comparison, we show several models that are excluded, given these fluxes. Detailed exclusion plots are found in the following sections. From a spectral fit with a generic power-law, $\propto \left(\frac{E_\gamma}{1\text{MeV}}\right)^\nu$, we derive an upper bound on the total flux in the band 20–8000 keV of $10^{-8}\,\text{erg}\,\text{cm}^{-2}\,\text{s}^{-1}$.

4.2 511 keV Line

We find a 511 keV line flux limit of $1.7\times10^{-4}\,\text{ph}\,\text{cm}^{-2}\,\text{s}^{-1}$. This value is about one order of magnitude smaller than the 3σ signal reported by Siegert et al. (2016c) of $(1.7 \pm 0.5) \times 10^{-3}\,\text{ph}\,\text{cm}^{-2}\,\text{s}^{-1}$. Given the enhanced exposure time and the source being inside the FCFOV all the time thanks to the new dedicated observation campaign, the improvement in sensitivity is plausible.

The previous detection of Ret II might be due to an intrinsic variability in time, as could be expected from the outburst of a micro-quasar (Siegert et al. 2016a) or a NS merger (Fuller et al. 2018),
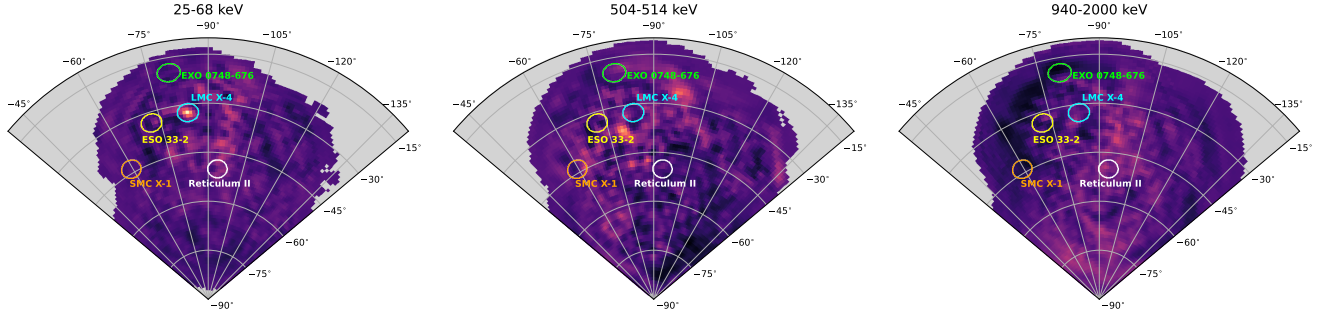
Figure 3. Count residuals projected back to the the sky by applying the imaging response backwards. The radial and azimuthal coordinates are the Galactic latitude and longitude, respectively. Shown are the bands 25–68 keV, 508–514 keV, and 940–2000 keV as examples. Only LMC X-4 is significantly detected in the first energy band.
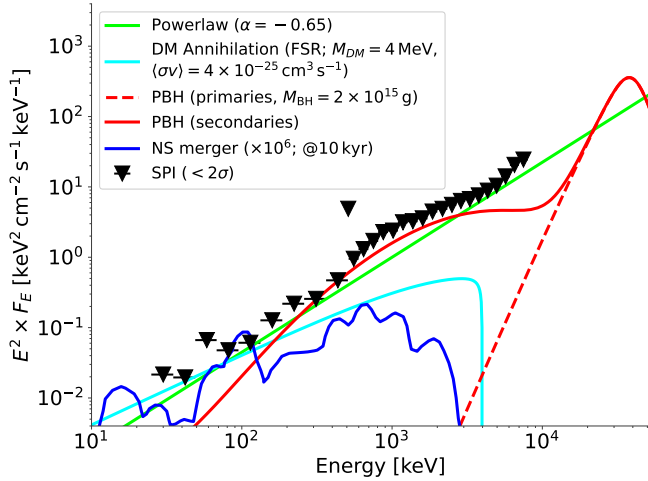

Figure 4. SPI spectrum from the position of Reticulum II. Shown are 2σ upper limits on the flux as a function of photon energy. A selection of excluded models is shown (see below).

for example. We therefore split the data set into different time bins according to chance observations of nearby targets as well as the new observation campaign. The resulting 511 keV light curve is shown in Fig. 5. Considering only observations in which Ret II is inside the FCFOV results in upper limits consistent with the previous measurement by Siegert et al. (2016c). We find that the significance of the 511 keV line rises up to $\sim 2\sigma$ until the end of the older data set. Including more data after 2013 and in particular the additional 1 Ms in 2018 (IJD ~ 6700), leads to a greatly reduced upper flux bound as well as a lower significance. Assuming the source to be variable in time, the upper limit on the 511 keV line is $\sim 6.1 \times 10^{-4}$ ph cm^{-2} s^{-1} – barely consistent with the previous estimate. We conclude that the 3σ signal from Ret II by Siegert et al. (2016c) was most likely due to an instrumental background fluctuation, paired with short exposures outside the FCFOV. We can not, however, exclude that the previously reported signal was of astrophysical origin.

4.3 Primordial Black Holes

We perform fits to the extracted spectrum, Fig. 4, with Eq. (21), and sub-cases thereof. Here we emphasise that we do *not* solve for the interesting parameters until a certain figure of merit is above a threshold, but determine the joint posterior distributions of all the free parameters in Eq. (21). That means we include the uncertainties on
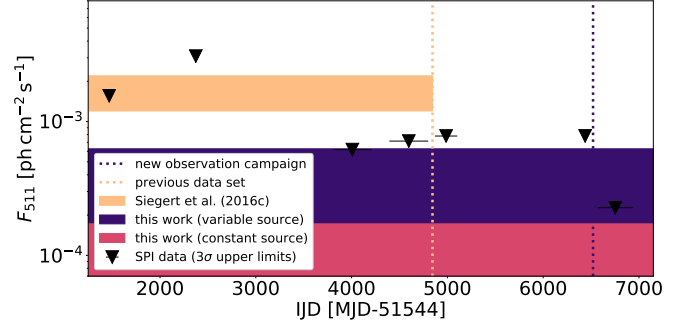

Figure 5. Lightcurve of the 511 keV line from Ret II. No positive excess is found at any time. Therefore, shown are 3σ upper limits in the band 508–514 keV. The inferred flux from Siegert et al. (2016c) is shown in comparison to the new INTEGRAL observation campaign. Additional serendipitous observations between IJD 4800 and 6600 are also included.

D and estimate f_{PBH} conditioned on all the other unknown parameters, and illustrate the limits on f_{PBH} as a function of M_{BH}, as it is typically done. However here we consider the 95th percentile in f_{PBH}-direction of the marginalised posterior $\pi(f_{\mathrm{PBH}}, M_{\mathrm{BH}}|y_i, \sigma_i)$ with y_i and σ_i as the flux values and corresponding uncertainties of energy bin i in the spectrum. See Appendix A for details. In Fig. 6, we show our upper bounds on f_{PBH}, and compare them to estimates from the recent literature, including the MW (Laha 2019; Laha et al. 2020), cosmic rays (Boudaud & Cirelli 2019), the cosmic microwave background (CMB, Clark et al. 2017), and the cosmic γ-ray background (CGB Iguaz et al. 2021).

The primary component of PBH evaporation alone cannot constrain f_{PBH} in Ret II. Including the secondary particles, the upper bound on $f_{\mathrm{PBH}} = 1$ excludes monochromatic PBH distributions with masses of $\lesssim 0.4 \times 10^{16}$ g. Assuming that all e^+s created by PBHs in Ret II annihilate strengthens the bound on f_{PBH}, then excluding masses $\lesssim 2.9 \times 10^{16}$ g. Since this assumption is too optimistic, we included the limiting factor for e^+ annihilation, that all e^+s above the threshold $E_{\mathrm{kin}}^{\mathrm{max}}$ escape from the galaxy and do not contribute to the annihilation spectrum. This describes our most realistic bound on $f_{\mathrm{PBH}} = 1$, which excludes masses $\lesssim 0.8 \times 10^{16}$ g.

Laha (2019) performed a similar estimate for the flux of the 511 keV line in the MW, however assumed that the entire annihilation flux, from integrating over the e^+-distribution of PBHs, ends up in the 511 keV line. Since the Ps fraction in the MW is within a range 0.97–1.00, the 511 keV line flux from PBHs is at least four times smaller, because most of the annihilation flux goes into the three-photon decay of ortho-Ps. In return this means that the bounds
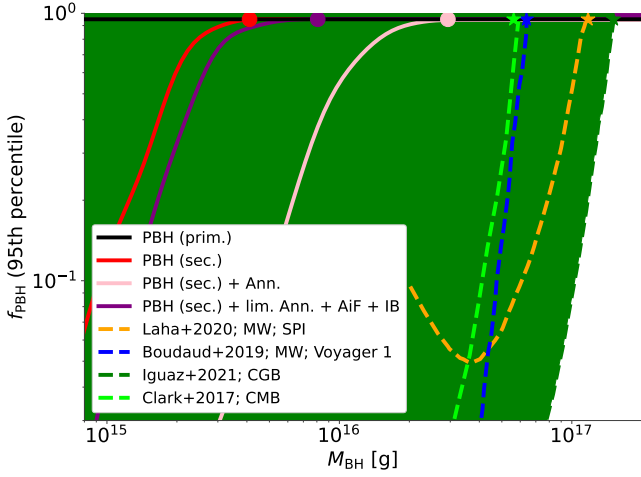
Figure 6. Fraction of DM that can be constituted of a monochromatic PBH distribution with mass M_{BH} in Ret II (solid lines), compared to literature estimates. The circles mark the masses when the 95th percentile of the posterior $\pi(f_{PBH}, M_{BH}|y_i, \sigma_i)$ in each case is reached. Stars mark the literature limits of 100 % PBH DM.

Figure 7. DM annihilation cross section into e^+e^- with subsequent FSR and possible annihilation of the pairs in Ret II (case 1. in Sec. 3.1.2; gray lines), compared to literature limits. The shaded regions are excluded.

Figure 8. Similar to Fig. 7 but for DM + DM $\rightarrow \gamma + \gamma$.

on f_{PBH} from Laha (2019) should be shifted by about a factor of four 'vertically', which decreases the mass at $f_{PBH} = 1$ from $\sim 8.9 \times 10^{16}$ g to $\sim 6.4 \times 10^{16}$ g. We test this by making the same assumptions with our Ret II spectrum, and find $f_{PBH} = 1$ is excluded for masses $M_{BH} \lesssim 4.0 \times 10^{16}$ g.

Our conservative and realistic bounds are about one order of magnitude in PBH mass below previous estimates. Nevertheless, our data set is considerably shorter than all the other data sets, often comprising more than a decade of observation time. Thanks to the much smaller region of interest in the case of Ret II, basically constituting a point source of SPI, our systematic uncertainties can be considered smaller compared to studies of the MW. The entire Galactic (DM) profile is rather uncertain, and also the Galactic centre itself bears problems when DM models are applied, as is often the case for diffuse emission in the GeV band. While our bounds are not yet as constraining, we show that reasonable progress can be made with even a small data set. In particular, we show that when all uncertainties on the spectral parameters are included also more conservative and realistic bounds can result.

4.4 Particle Dark Matter

Similar to the PBH case, we perform a fit to the extracted Ret II spectrum and marginalise over the uncertain parameters to determine the posteriors $\pi(\langle\sigma v\rangle, m_{DM}|y_i, \sigma_i)$ and $\pi(\tau, m_{DM}|y_i, \sigma_i)$ for DM annihilation and decay, respectively. In what follows, the excluded regions consider the 95th percentile of the posteriors in $\langle\sigma v\rangle$- and τ-direction, respectively.

4.4.1 Annihilation

In Fig. 7, we show the excluded region of the velocity-averaged DM annihilation cross section into e^+e^-, followed by FSR and subsequent e^+ annihilation. Without additional e^+ annihilation, the bounds from Ret II are barely comparable to literature values from other γ-ray experiments (Essig et al. 2013) or the CMB (Slatyer 2016). When limited e^+ annihilation is included, we can improve the limits in the DM mass range 0.5–1.0 MeV, and find
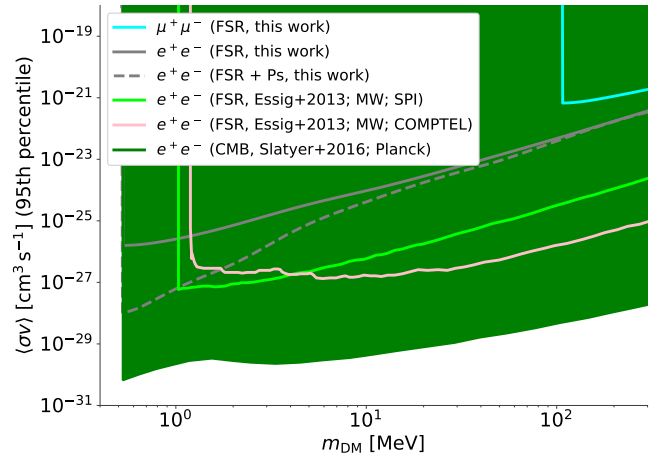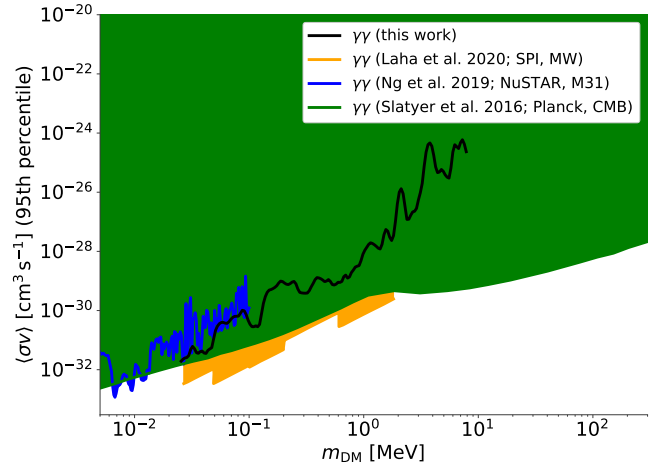
a general trend of the annihilation cross section at tree level of $\langle\sigma v\rangle \lesssim 5 \times 10^{-28} (m_{DM}/\text{MeV})^{2.5}$ cm³ s⁻¹, based on the shape of the measured limits as a function of energy in Fig. 7. For completeness, we show the limits on DM annihilation into $\mu^+\mu^-$, being hardly constrained by Ret II data.

The cross section limit for the case DM + DM $\rightarrow \gamma + \gamma$ is shown in Fig. 8. Our limits on DM annihilation into two photons are comparable to those from NuSTAR observations of M31 (Ng et al. 2019), and about one order of magnitude worse than from MW observations with SPI (Laha et al. 2020). Because our data set extends to the full energy range of SPI, we can set however limits out to $m_{DM} \leq 8$ MeV, varying between 10^{-28} and 10^{-25} cm³ s⁻¹. However, limits from the CMB (Slatyer 2016) are still more stringent at there energies.

4.4.2 Decay

The properties of decaying DM particles cannot be inferred directly from the previous case of annihilating DM. First, the kinematic thresholds for standard model particle production is shifted by a factor of two which leads to altered (shifted) spectral shapes in particular for FSR and IA. Second, the J-factor of Ret II is about twice as
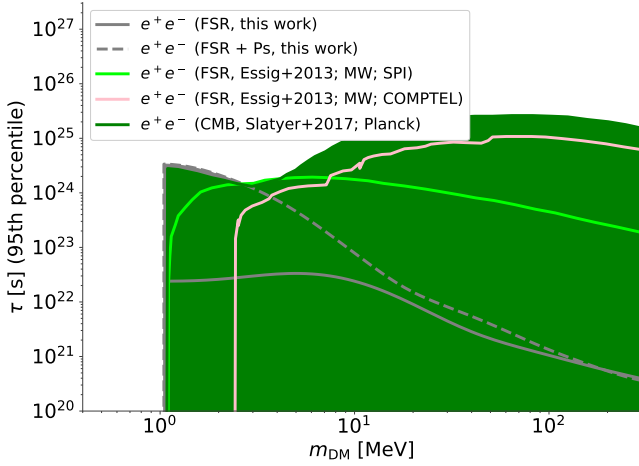
Figure 9. Similar to Fig. 7 but for DM $\rightarrow$ e$^+$ + e$^-$ + (γ)$_{\rm FSR}$.
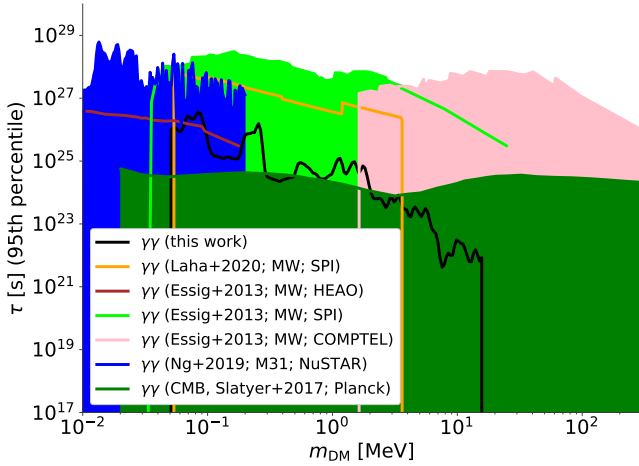
Figure 10. Similar to Fig. 7 but for DM $\rightarrow \gamma + \gamma$. For the case DM $\rightarrow \gamma +$ Y, the limits are smaller by a factor of 2.

uncertain as its D-factor, which allows to populate different regions in the full posterior. We therefore perform spectral fits for the DM decay case separately to infer bounds on the DM lifetime τ. This also results in slightly worse bounds when considering decay compared to annihilation (cf. NuSTAR limits).

In Fig. 9 we show the the exclusion region of τ as a function of the DM mass. Similar to the DM annihilation case, FSR alone is barely constraining, but can be pushed by including e$^+$ annihilation. We find that DM particles decaying into e$^+$e$^-$ pairs must have a lifetime longer than 1–5×10^{24} s between 1 and 2 MeV. In the mass range 1–2 MeV, our bounds are as strong as the limits from the CMB Slatyer & Wu (2017). Above this mass range, previous limits from SPI and COMPTEL in the MW (Essig et al. 2013), and in particular those from the CMB are more constraining.

Finally, our DM decay time limits considering the direct decay into two photons is not improving beyond previous constraints. This is expected from the pure narrow line sensitivity of SPI.

5 SUMMARY AND CONCLUSION

Ret II is not seen in soft γ-rays between 0.025 and 8 MeV, up to an upper flux limit of 10^{-8} erg cm^{-2} s^{-1} (5×10^{-10} erg cm^{-2} s^{-1} within 20–80 keV). The previously reported 511 keV line signal in Ret II has not been consolidated in this work, and we provide an upper limit on its flux of 1.7×10^{-4} ph cm^{-2} s^{-1}. Given the distance to the galaxy, this constrains the e$^+$-annihilation rate (including Ps formation and annihilation in flight) to 0.9–3.7×10^{43} e$^+$ s^{-1}, at most the annihilation rate of the MW[1].

We calculated parametrised spectral models for PBH evaporation and DM annihilation/decay with subsequent e$^+$ annihilation and fitted these models to the total spectrum from Ret II. Our conservative limit on the monochromatic PBH mass distribution constituting the entirety of DM in Ret II is 0.8×10^{16} g. We improve the limits on the velocity-averaged DM annihilation cross section of decay time of DM particles into e$^+$e$^-$ in the range 0.5–2 MeV. For annihilation or decay into two photons, our limits are weaker than previous estimates. We provide the currently only limits on the cross section $\langle \sigma v \rangle_{\gamma\gamma}$ in the range 3–8 MeV, ranging between 10^{-28} and 10^{-25} cm^3 s^{-1}.

While our estimates are at most on the same level as previous constraints, we arrive at our conclusions with a very small data set (two weeks) compared to the multi-year or even decade-long observations. With our detailed spectral modelling including the effects of possible e$^+$ annihilation and the proper statistical treatment of known unknowns, we show that dedicated observations of selected targets provide valuable information about the DM conundrum. We encourage follow-up observations of Ret II and other dwarf galaxies with INTEGRAL, and foresee a bright future for soft γ-ray instruments to come, such as COSI (Tomsick et al. 2019), to contribute significantly in the research for the nature of DM.

DATA AVAILABILITY

The data underlying this article will be shared on reasonable request to the corresponding author.

---

[1] We note that in Siegert et al. (2016c), there is a typo, reducing the estimate for Ret II by a factor of ten – the actual annihilation rate in the previous work should be on the order of 10^{44} e$^+$ s^{-1}.

REFERENCES

Albert A., et al., 2017, The Astrophysical Journal, 834, 110

Arbey A., Auffinger J., 2019, The European Physical Journal C, 79, 693

Attié D., et al., 2003, Astronomy & Astrophysics, 411, L71

Beacom J. F., Yüksel H., 2006, Physical Review Letters, 97, 071102

Beacom J. F., Bell N. F., Bertone G., 2005, Physical Review Letters, 94, 171301

Boehm C., Hooper D., Silk J., Cassé M., Paul J., 2004, Physical Review Letters, 92, 101301

Bonnivard V., et al., 2015, The Astrophysical Journal Letters, 808, L36

Boudaud M., Cirelli M., 2019, Physical Review Letters, 122, 041104

Churazov E., Sunyaev R., Sazonov S., Revnivtsev M., Varshalovich D., 2005, Monthly Notices of the Royal Astronomical Society, 357, 1377

Churazov E., Sazonov S., Tsyganков S., Sunyaev R., Varshalovich D., 2011, Monthly Notices of the Royal Astronomical Society, 411, 1727

Clark S. J., Dutta B., Gao Y., Strigari L. E., Watson S., 2017, Physical Review D, 95, 083006

Collaboration A., et al., 2013, Astronomy & Astrophysics, 558, A33

Cordier B., et al., 2004, in Schoenfelder V., Lichti G., Winkler C., eds, 5th INTEGRAL Workshop on the INTEGRAL Universe. p. 581

Diehl R., et al., 2018, Astronomy & Astrophysics, 611, A12

Essig R., Kuflik E., McDermott S. D., Volansky T., Zurek K. M., 2013, Journal of High Energy Physics, 11, 193

Evans N. W., Sanders J. L., Geringer-Sameth A., 2016, arXiv, 93, 103512

Feroz F., Hobson M. P., 2008, Monthly Notices of the Royal Astronomical Society, 384, 449

Feroz F., Hobson M. P., Bridges M., 2009, Monthly Notices of the Royal Astronomical Society, 398, 1601

Feroz F., Hobson M. P., Cameron E., Pettitt A. N., 2019, The Open Journal of Astrophysics, 2, 10

Fortin J.-F., Shelton J., Thomas S., Zhao Y., 2009, arXiv.org, p. arXiv:0908.2258

Fuller G. M., Kusenko A., Radice D., Takhistov V., 2018, arXiv.org

Geringer-Sameth A., Walker M. G., Koushiappas S. M., Koposov S. E., Belokurov V., Torrealba G., Evans N. W., 2015, Physical Review Letters, 115, 081101

Halloin H., 2009, |spimodfit| Explanatory Guide and Users Manual. Max Planck Institut für extraterrestrische Physik Max Planck Institut für extraterrestrische Physik, Giessenbachstraße 1, 85748 Garching, Germany, version 2.9 edn

Hawking S. W., 1975, Communications In Mathematical Physics, 43, 199

Hunter J. D., 2007, Computing in Science & Engineering, 9, 90

Iguaz J., Serpico P. D., Siegert T., 2021, arXiv.org, p. arXiv:2104.03145

Jean P., Knoedlseder J., Gillard W., Guessoum N., Ferrière K., Marcowith A., Lonjou V., Roques J. P., 2006, Astronomy & Astrophysics, 445, 579

Koposov S. E., Belokurov V., Torrealba G., Evans N. W., 2015, arXiv.org, 805, 130

Korobkin O., et al., 2020, The Astrophysical Journal, 889, 168

Laha R., 2019, Physical Review Letters, 123, 251101

Laha R., Muñoz J. B., Slatyer T. R., 2020, Physical Review D, 101, 123514

Leventhal M., MacCallum C. J., Stang P. D., 1978, Astrophysical Journal, 225, L11

Ng K. C. Y., Roach B. M., Perez K., Beacom J. F., Horiuchi S., Krivonos R., Wik D. R., 2019, Physical Review D, 99, 083005

Oliphant T. E., 2006, A guide to NumPy. Vol. 1, Trelgol Publishing USA

Ore A., Powell J. L., 1949, Physical Review, 75, 1696

Page D. N., Hawking S. W., 1976, Astrophysical Journal, 206, 1

Siegert T., et al., 2016a, Nature, 531, 341

Siegert T., Diehl R., Khachatryan G., Krause M. G. H., Guglielmetti F., Greiner J., Strong A. W., Zhang X., 2016b, Astronomy & Astrophysics, 586, A84

Siegert T., Diehl R., Vincent A. C., Guglielmetti F., Krause M. G. H., Boehm C., 2016c, Astronomy & Astrophysics, 595, A25

Siegert T., Diehl R., Weinberger C., Pleintinger M. M. M., Greiner J., Zhang X., 2019, Astronomy & Astrophysics, 626, A73

Sizun P., Cassé M., Schanne S., 2006, Phys. Rev. D, 74, 063514

Slatyer T. R., 2016, Physical Review D, 93, 023527

Slatyer T. R., Wu C.-L., 2017, Physical Review D, 95, 023010

Svensson R., 1982,] 10.1086/160081, 258, 321

Tomsick J. A., et al., 2019, arXiv.org, p. arXiv:1908.04334

Vedrenne G., et al., 2003, Astronomy & Astrophysics, 411, L63

Vianello G., et al., 2015, arXiv.org, p. arXiv:1507.08343

Virtanen P., et al., 2019, arXiv.org, p. arXiv:1907.10121

Winkler C., et al., 2003, Astronomy & Astrophysics, 411, L1

APPENDIX A: DETAILS ON SPECTRAL FITS

The error bars in the extracted spectrum in Sec. 4.1, Fig. 4 approximately follow a normal distribution. Therefore, we use the likelihood

$$\mathscr{L}_{\mathrm{normal}}(D|M(\psi)) = \prod_{i=1}^{30} \frac{1}{\sqrt{2\pi}\sigma_i} \exp\left(-\frac{1}{2}\left[\frac{y_i - m_i(\psi)}{\sigma_i}\right]^2\right), \quad \text{(A1)}$$

with y_i as the measured flux in energy bin $i = 1 \ldots 30$ in the spectrum, σ_i the corresponding uncertainties, and $m_i(\psi)$ the forward-folded model, Eq. (4), that depends on a set of spectral parameters ψ.

Since we want to include the astrophysical and particle physics uncertainties of our source, we construct the joint posterior of all N parameters $\psi_1 \ldots \psi_N$ through Bayes' theorem as

$$\pi(\psi_1 \ldots \psi_N|y_i, \sigma_i) \propto \mathscr{L}_{\mathrm{normal}}(y_i, \sigma_i|\psi_1 \ldots \psi_N)\pi(\psi_1 \ldots \psi_N). \tag{A2}$$

Here, $\pi(\psi_1 \ldots \psi_N)$ is the joint prior distribution of the individual parameters. We use independent priors so that $\pi(\psi_1 \ldots \psi_N) = \pi(\psi_1) \cdots \pi(\psi_N)$, that is, each parameter obtains its individual prior probability distribution function. By integrating out the parameters ψ_3 to ψ_N, for example, we can construct the marginalised joint posterior distribution of ψ_1 and ψ_2,

$$\pi(\psi_1, \psi_2|y_i, \sigma_i) = \int \cdots \int d\psi_2 \cdots \psi_N \pi(\psi_1 \ldots \psi_N|y_i, \sigma_i). \text{ (A3)}$$

To obtain the upper bound on ψ_1 as a function of ψ_2, we integrate the marginalised posterior $\pi(\psi_1, \psi_2|y_i, \sigma_i)$ in ψ_1-direction and equate to a certain percentile P,

$$P = \int_{\psi_1^{\mathrm{min}}}^{\psi_1^{\mathrm{ub}}(\psi_2)} d\psi_1 \pi(\psi_1, \psi_2|y_i, \sigma_i). \tag{A4}$$

Solving Eq. (A4) for $\psi_1^{\mathrm{ub}}(\psi_2)$ provides the upper bound on ψ_1 as function of ψ_2.

A written example considering the case of annihilating DM into e^+e^- with subsequent FSR and e^+ annihilation would calculate the upper bound on the velocity-averaged annihilation cross section $\langle\sigma v\rangle$ as a function of the DM mass m_{DM}. Thus first, the join posterior $\pi(\langle\sigma v\rangle, m_{\mathrm{DM}}, J, f_{\mathrm{Ps}}, E_{\mathrm{kin}}^{\mathrm{max}}|y_i, \sigma_i)$ is estimated, then marginalised over the J-factor, the Ps fraction and the kinetic energy threshold to avoid escape,

$$\pi(\langle\sigma v\rangle, m_{\mathrm{DM}}|y_i, \sigma_i) =$$
$$\int_{J_{\mathrm{min}}}^{J_{\mathrm{max}}} dJ \int_{f_{\mathrm{Ps,min}}}^{f_{\mathrm{Ps,max}}} df_{\mathrm{Ps}} \int_{E_{\mathrm{kin,min}}^{\mathrm{max}}}^{E_{\mathrm{kin,max}}^{\mathrm{max}}} dE_{\mathrm{kin}}^{\mathrm{max}}$$
$$\pi(\langle\sigma v\rangle, m_{\mathrm{DM}}, J, f_{\mathrm{Ps}}, E_{\mathrm{kin}}^{\mathrm{max}}|y_i, \sigma_i), \tag{A5}$$

and finally integrated up to the bound $\langle\sigma v\rangle^{\mathrm{ub}}(m_{\mathrm{DM}})$ by

$$P = \int_0^{\langle\sigma v\rangle^{\mathrm{ub}}(m_{\mathrm{DM}})} d\langle\sigma v\rangle \pi(\langle\sigma v\rangle, m_{\mathrm{DM}}|y_i, \sigma_i). \tag{A6}$$

We use MultiNest (Feroz & Hobson 2008; Feroz et al. 2009, 2019)
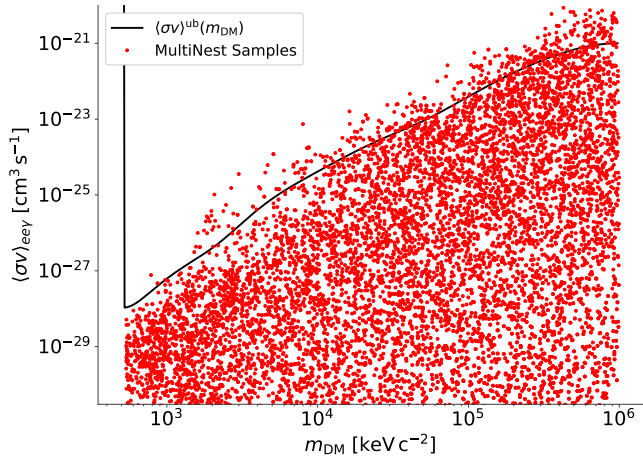
Figure A1. Marginalised posterior distribution $\pi(\langle\sigma v\rangle, m_{\mathrm{DM}}|y_i, \sigma_i)$ (red dots), together with upper bounds of the annihilation cross section as a function of the DM mass (black line).

in 3ML to evaluate the joint posterior distributions, marginalisations, and upper bounds. We show the samples of this example in Fig. A1. We list our prior distributions and parameter ranges for all considered models in Tab. A1.

This paper has been typeset from a TEX/LATEX file prepared by the author.

Model	κ	M	D	J	$f_{\rm Ps}$	$E_{\rm kin}^{\rm max}$
PBH (prim.)	$\mathscr{U}(0,1)$	$\log\mathscr{U}(10^{14},10^{18})$	$\mathscr{U}(10^{18},4\times10^{18})$	–	–	–
PBH (sec.)	⋮	⋮	⋮	–	–	–
PBH (sec.) + Ann.	⋮	⋮	⋮	–	$\mathscr{U}(0,1)$	–
PBH (sec.) + lim. Ann.	⋮	⋮	⋮	–	⋮	$\log\mathscr{U}(10^{3},10^{5})$
2DM $\to$ e$^+$e$^-\gamma$	$\log\mathscr{U}(3\times10^{-34},3\times10^{-20})$	$\log\mathscr{U}(511,10^{6})$	–	$\mathscr{U}(2\times10^{18},4\times10^{19})$	$\mathscr{U}(0,1)$	$\log\mathscr{U}(10^{3},10^{5})$
2DM $\to 2\gamma$	⋮	$\log\mathscr{U}(25,8000)$	–	⋮	–	–
DM $\to$ e$^+$e$^-\gamma$	$\log\mathscr{U}(10^{15},10^{24})$	$\log\mathscr{U}(1022,10^{6})$	$\mathscr{U}(10^{18},4\times10^{18})$	–	$\mathscr{U}(0,1)$	$\log\mathscr{U}(10^{3},10^{5})$
DM $\to 2\gamma$	$\log\mathscr{U}(10^{15},10^{29})$	$\log\mathscr{U}(50,16000)$	⋮	–	–	–

Table A1. Prior distributions for considered DM models in Eq. (5).